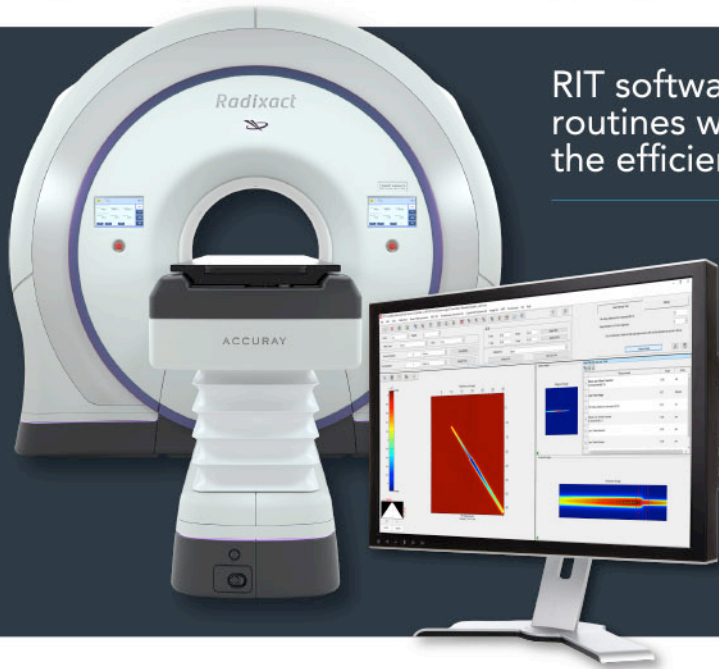


COMPREHENSIVE TG-148 QA SOLUTIONS

FROM RADIOLOGICAL IMAGING TECHNOLOGY, INC.

RIT offers two software packages for comprehensive TG-148 QA of helical tomotherapy machines. RITG148+ is a precise and state-of-the-art software built to perform all machine and imaging QA measurements for TomoTherapy® and Radixact® treatment delivery systems. RIT Complete adds patient QA capabilities by providing an advanced TomoTherapy Registration feature.

RITG148+
AND
RIT Complete



RIT software's combination of innovative, robust routines with a user-friendly interface to maximize the efficiency and precision of your measurements.

Designed in accordance with TG-148 guidelines, the RITG148+ and RIT Complete software packages analyze the standardized tests and all others recommended for daily, monthly, and annual QA of tomotherapy machines. This includes Static & Rotational Output Consistency, Jaw Centering & Alignment, Overhead Laser Positioning, Interrupted Treatment, and all others recommended for daily, monthly, and annual QA. RITG148+ also analyzes image quality using the tomotherapy cheese phantom.

Automated QA Tests

- Y-jaw/gantry rotation plane alignment
- Y-jaw divergence/beam centering
- Couch translation/gantry rotation
- Gantry angle consistency
- Treatment field centering
- Interrupted treatment
- MLC alignment test
- Laser localization

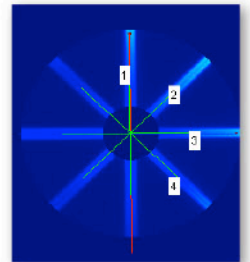
TomoTherapy® Registration*

Upgrade to RIT Complete to perform TomoTherapy® patient QA in addition to all the machine and imaging QA tests already included in RITG148+. Easily perform exact dose comparisons using a TomoTherapy® plan, a dose map, and a film to determine position and dose accuracy using the red or green lasers. Coronal and sagittal slices may be analyzed.

*Only available in the RIT Complete software package.

Image Quality Tests

- Noise
- Contrast
- Resolution
- Uniformity
- Geometric Accuracy
- Geometric Distortion
- CT Number to Density
- Pin Prick, Erase, and ROI tool



Built-In Features

-  RITtrend™ statistical database for reporting and trending measurements over time
-  PDF report exports for every analysis routine

**CLICK TO REQUEST A DEMO
& UPGRADE YOUR TG-148
QA CAPABILITIES TODAY**



RADIMAGE.COM

+1.719.590.1077, Opt. 4 // sales@radimage.com // Connect with us on social media @RIT4QA

©2021, Radiological Imaging Technology, Inc.

TomoTherapy® and Radixact® are registered trademarks of Accuray, Inc.

Experiments and Monte Carlo simulations on multiple Coulomb scattering of protons

Nico Verbeek^{a)}

West German Proton Therapy Centre Essen WPE, Essen, Germany
Faculty of Medicine, University of Duisburg-Essen, Essen, Germany
University Hospital Essen, West German Cancer Center WTZ, Essen, Germany

Jörg Wulff

West German Proton Therapy Centre Essen WPE, Essen, Germany
University Hospital Essen, West German Cancer Center WTZ, Essen, Germany

Martin Janson

RaySearch Laboratories, Stockholm, Sweden

Christian Bäumer

West German Proton Therapy Centre Essen WPE, Essen, Germany
University Hospital Essen, West German Cancer Center WTZ, Essen, Germany
Radiation Oncology and Imaging, German Cancer Consortium DKTK, Heidelberg, Germany
Technische Universität Dortmund, Otto-Hahn-Str. 4a, Dortmund 44227, Germany

Sameera Zahid

West German Proton Therapy Centre Essen WPE, Essen, Germany
Carl von Ossietzky Universität Oldenburg, Oldenburg, Germany

Beate Timmermann

West German Proton Therapy Centre Essen WPE, Essen, Germany
Faculty of Medicine, University of Duisburg-Essen, Essen, Germany
University Hospital Essen, West German Cancer Center WTZ, Essen, Germany
Radiation Oncology and Imaging, German Cancer Consortium DKTK, Heidelberg, Germany
Department of Particle Therapy, University Hospital Essen, Essen, Germany

Lorenzo Brualla

West German Proton Therapy Centre Essen WPE, Essen, Germany
Faculty of Medicine, University of Duisburg-Essen, Essen, Germany
University Hospital Essen, West German Cancer Center WTZ, Essen, Germany

(Received 25 November 2020; revised 10 March 2021; accepted for publication 18 March 2021; published xx xxxx xxxx)

Background and purpose: Monte Carlo simulations as well as analytical computations of proton transport in material media require accurate values of multiple Coulomb scattering (MCS) angles. High-quality experimental data on MCS angles in the energy range for proton therapy are, however, sparse. In this work, MCS modeling in proton transport was evaluated employing an experimental method to measure these angles on a medical proton beamline in clinically relevant materials. Results are compared to Monte Carlo simulations and analytical models.

Materials and methods: Aluminum, brass, and lucite (PMMA) scatterers of clinically relevant thicknesses were irradiated with protons at 100, 160, and 220 MeV. Resulting spatial distributions of individual pencil beams were measured with a scintillating screen. The MCS angles were determined by deconvolution and a virtual point source approach. Results were compared to those obtained with the Monte Carlo codes PENH, TOPAS, and RayStation Monte Carlo, as well as the analytical models RayStation Pencil Beam Algorithm and the Molière/Fano/Hanson variant of the Molière theory.

Results: Experimental data obtained with the presented methodology agree with previously published results within 6%, with an average deviation of 3%. The combined average uncertainty of the experimental data yielded 1.8%, while the combined maximum uncertainty was below 4%. The obtained Monte Carlo results for PENH, TOPAS, and RayStation deviate on average for all considered energies, materials and thicknesses, by 2.5%, 3.4%, and 2.8% from the experimental data, respectively. For the analytical models, the average deviations amount to 4.5% and 2.9% for the RayStation Pencil Beam Algorithm and the Molière/Fano/Hanson model, respectively.

Conclusion: The experimental method developed for the present work allowed to measure MCS angles in clinical proton facilities with good accuracy. The presented method permits to extend the database on experimental MCS angles which is rather limited. This work further provides benchmark data for lucite in thicknesses relevant for clinical applications. The data may serve to validate dose engines of treatment planning systems and secondary dose check software. The Monte Carlo and

analytical algorithms studied are capable of reproducing MCS data within the required accuracy for clinical applications. © 2021 The Authors. *Medical Physics* published by Wiley Periodicals LLC on behalf of American Association of Physicists in Medicine [https://doi.org/10.1002/mp.14860]

Key words: Geant4, Monte Carlo, multiple scattering, PENELOPE, PENH, proton, TOPAS

1. INTRODUCTION

Multiple Coulomb scattering (MCS) theory is employed to predict the angular distribution of charged particles scattered in matter. In pencil-beam scanning proton therapy, the beam is scattered when, for example, traversing lucite range shifters and beam shaping apertures made of brass or within the patient itself. Over the years, multiple analytical approaches have been developed to predict the angular distribution of protons in MCS theory. The work of Molière/Fano^{1,2} with Hanson's³ modifications has been extensively used.⁴⁻⁶ At energies and scatterer thicknesses relevant in proton therapy, the angular distribution can be approximated by a Gaussian.⁷

The accurate calculation of MCS angles is crucial for the computation of absorbed dose distributions performed by treatment planning systems (TPS) and radiation transport Monte Carlo codes. An over or underestimation of the MCS angle may lead to an under or overestimation of the deposited energy in a given region. For example, a flaw in the semi-empirical calculation of MCS in range shifters for a previous version of the Eclipse proton TPS led to spot-size deviations up to 20%.⁸ Concurrently, Monte Carlo simulations also depend on MCS theories to implement the condensed history approach that notably increases simulation efficiency. Therefore, it is of utmost importance to shed light on the accuracy of MCS angle calculation in materials and energies relevant in proton therapy.

Despite the fundamental importance of these data, there is only a limited amount of experimental MCS angles available in the aforementioned conditions. The most detailed dataset provided in recent times for 160 MeV was published by Gottschalk et al. in 1993.⁷ Since then, this dataset has been used as the main reference. For example, the MCS implementation in the Monte Carlo code Geant4^{9,10} was recently benchmarked by Makarova et al.⁶ and Fuchs et al.¹¹

The purpose of the present work is to develop an experimental method to measure MCS angles at a proton therapy facility. As a result, the existing dataset is extended for therapeutically relevant materials and energies and compared to the well-established Monte Carlo code TOPAS v3.2p1 (Geant4),¹² the TPS RayStation 9B with RayStation Monte Carlo 4.5,¹³ the RayStation Pencil Beam Algorithm 5.1¹³ and PENH 2020.¹⁴ PENH is the recently coded and benchmarked¹⁵ extension to the mixed class II¹⁶ algorithm PENELOPE^{17,18} to incorporate proton nuclear interactions. Additionally, the results are compared to the analytical Molière/Fano/Hanson model, as implemented in the freely distributed software LOOKUP.^{6,19}

2. MATERIAL AND METHODS

In this work, a nomenclature similar to that employed by Gottschalk et al.,⁷ Makarova et al.,⁶ and Fuchs et al.¹¹ is used. The standard deviation of the experimental MCS angle distribution is θ_0 . According to the respective Monte Carlo simulations and analytical models, θ_P , θ_T , θ_{RSMC} , θ_{RSPBA} , and θ_{MFH} are the MCS angles obtained from simulations using PENH, TOPAS, RayStation Monte Carlo, RayStation Pencil Beam Algorithm and the Molière/Fano/Hanson angles. The experiments and simulations were conducted for the three nominal energies 100, 160, and 220 MeV and for the materials aluminum, brass, and lucite.

To facilitate comparison among energies, thicknesses, and material densities, the three quantities have been combined into a dimensionless factor analogue to the one employed by Gottschalk et al.⁷

$$t_\rho \equiv \frac{t}{R}\rho, \quad (1)$$

where R is the mean projected range, t is the physical thickness of the scatterer, and ρ is the mass density. The values for R were calculated using the LOOKUP software. All combinations of ranges energies, materials, thicknesses, material compositions, and mean excitation energies are included in Table I.

2.A. Experimental setup

The experiments were performed at the West German Proton Therapy Centre Essen (WPE) with an IBA ProteusPlus (IBA PT, Louvain-la-Neuve, Belgium) treatment system, which consists of an isochronous cyclotron that accelerates protons to an energy of 228 MeV. Lower energies are achieved by degradation of the beam employing wheel-mounted wedges. The experiments were performed on the horizontal beamline, which is equipped with a universal nozzle used in pencil-beam scanning mode. The scatterers for the experiments were attached to the universal nozzle using the snout holder.

A single finite spot size proton pencil beam (from now on referred to as pencil beam) impinged on the scatterer using all combinations of thickness, energy and material according to Table I (Fig. 1). In addition to the scattered beam profiles (F_{total}), scatterer-free beam profiles (F_{initial}) were measured at the three energies used.

The flux profiles for calculating θ_0 were measured using the Lynx PT detector (IBA Dosimetry, Schwarzenbruck, Germany).²⁰ The Lynx PT has an active area of $30 \times 30 \text{ cm}^2$ with a pixel pitch of 0.5 mm. To change the amount of light reaching the CCD, it is possible to set a variable aperture of the collimator system between 0 and 100 (iris setting).^{21,22} The measuring

TABLE I. Material compositions for the Monte Carlo simulations, and scatterer thicknesses t used at the respective energies and conversion to the dimensionless thickness range relation t_ρ .

| 100 MeV | | | 160 MeV | | | 220 MeV | | |
|---------------------------------------|-------------------------------|----------|-----------------------------|-------------------------------|----------|------------------------|-------------------------------|----------|
| Al | | | | | | | | |
| $\rho_{Al} = 2.70 \text{ g/cm}^3$ | | | | | | $I = 166.0 \text{ eV}$ | | |
| $R = 10.01 \text{ g/cm}^2$ | | | 22.72 g/cm^2 | | | 39.16 g/cm^2 | | |
| t [cm] | t_ρ [g/cm ²] | t_ρ | t [cm] | t_ρ [g/cm ²] | t_ρ | t [cm] | t_ρ [g/cm ²] | t_ρ |
| 0.70 | 1.89 | 0.19 | 0.70 | 1.89 | 0.08 | 1.50 | 4.05 | 0.10 |
| 1.50 | 4.05 | 0.40 | 1.50 | 4.05 | 0.18 | 3.00 | 8.10 | 0.21 |
| 2.50 | 6.75 | 0.67 | 3.50 | 9.45 | 0.42 | 6.00 | 16.20 | 0.41 |
| 3.00 | 8.10 | 0.81 | 5.00 | 13.50 | 0.59 | 9.00 | 24.30 | 0.62 |
| – | – | – | 6.00 | 16.20 | 0.71 | 11.00 | 29.70 | 0.76 |
| Brass | | | | | | | | |
| $\rho_{Brass} = 8.47 \text{ g/cm}^3$ | | | 58% Cu, 39% Zn, 3% Pb | | | $I = 333.2 \text{ eV}$ | | |
| $R = 11.92 \text{ g/cm}^2$ | | | 26.81 g/cm^2 | | | 45.87 g/cm^2 | | |
| t [cm] | t_ρ [g/cm ²] | t_ρ | t [cm] | t_ρ [g/cm ²] | t_ρ | t [cm] | t_ρ [g/cm ²] | t_ρ |
| 0.50 | 4.24 | 0.36 | 0.50 | 4.24 | 0.16 | 0.70 | 5.93 | 0.13 |
| 0.80 | 6.78 | 0.57 | 0.70 | 5.93 | 0.22 | 1.00 | 8.47 | 0.18 |
| 1.00 | 8.47 | 0.71 | 1.50 | 12.71 | 0.47 | 2.00 | 16.94 | 0.37 |
| – | – | – | 2.00 | 16.94 | 0.63 | 3.00 | 25.41 | 0.55 |
| – | – | – | 2.50 | 21.18 | 0.79 | 4.00 | 33.88 | 0.74 |
| Lucite | | | | | | | | |
| $\rho_{Lucite} = 1.19 \text{ g/cm}^3$ | | | 8.05% H, 59.98% C, 31.96% O | | | $I = 74.0 \text{ eV}$ | | |
| $R = 7.93 \text{ g/cm}^2$ | | | 18.14 g/cm^2 | | | 31.39 g/cm^2 | | |
| t [cm] | t_ρ [g/cm ²] | t_ρ | t [cm] | t_ρ [g/cm ²] | t_ρ | t [cm] | t_ρ [g/cm ²] | t_ρ |
| 1.50 | 1.79 | 0.23 | 2.16 | 2.57 | 0.14 | 3.00 | 3.57 | 0.11 |
| 2.50 | 2.98 | 0.38 | 3.00 | 3.57 | 0.20 | 5.00 | 5.95 | 0.19 |
| 3.00 | 3.57 | 0.45 | 4.44 | 5.28 | 0.29 | 10.00 | 11.90 | 0.38 |
| 4.00 | 4.76 | 0.60 | 5.00 | 5.95 | 0.33 | 15.00 | 17.85 | 0.57 |
| 5.00 | 5.95 | 0.75 | 6.00 | 7.14 | 0.39 | 20.00 | 23.80 | 0.76 |
| – | – | – | 6.42 | 7.64 | 0.42 | – | – | – |
| – | – | – | 9.00 | 10.71 | 0.59 | – | – | – |
| – | – | – | 12.00 | 14.28 | 0.79 | – | – | – |

plane of the Lynx PT was aligned perpendicular to the proton beam at a distance $z_{MP} = 81 \text{ cm}$ from the upstream surface of the scatterer using orthogonal x rays (positional accuracy 0.5 mm). The sensitivity of the CCD detector (iris setting of the camera aperture) of the Lynx PT detector was kept constant during measurements. To ensure a signal intensity level at $\approx 80\%$, while keeping the iris setting constant, monitor units (MUs) varied according to the energy of the pencil beam and to the thickness and density of the scatterer.

2.B. Methodology for the analysis of the experimental and TPS results

The shape of the angular distribution of the scattered proton beam is often approximated by a normal distribution taking

into account $\approx 96\%$ of the protons.⁶ This core area dominates the calculation of the proton dose in radiation therapy. Since the Molière single scattering tail only becomes relevant for scattering angles θ larger than ≈ 2.5 times the standard deviation θ_0 of the angular distribution, the MCS angle can be approximated using the Molière/Fano/Hanson theory.^{6,7} Therefore, the scattered angles from the measurements and the simulations are considered to be normally distributed.

Accordingly, the measured profiles were fitted with two one-dimensional (1D) normal distributions,

$$F_{\text{total}}(r) = A_{\text{total}} \exp\left[-(r - r_{\text{ctotal}})^2 / (2\sigma_{\text{total}}^2)\right] \quad \text{and} \quad (2)$$

$$F_{\text{initial}}(r) = A_{\text{initial}} \exp\left[-(r - r_{\text{cinitial}})^2 / (2\sigma_{\text{initial}}^2)\right], \quad (3)$$

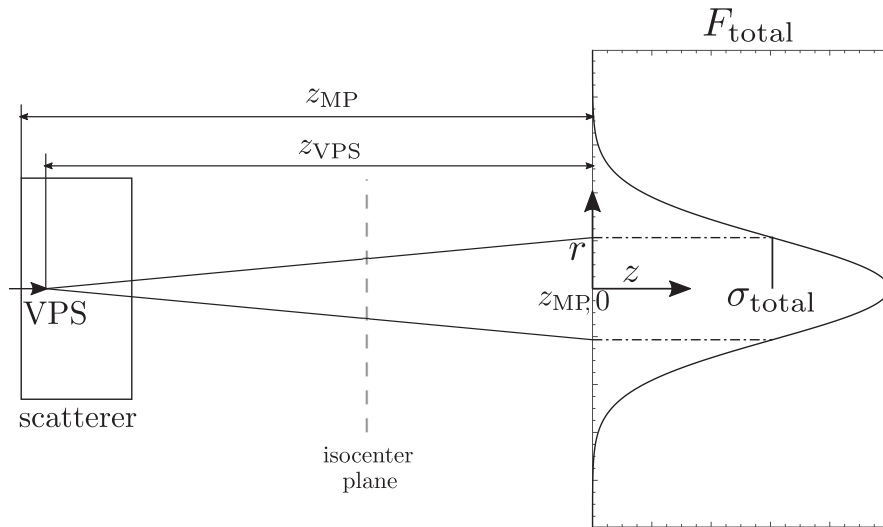


FIG. 1. Schematic representation of the MCS angle calculation. The distance between the scatterer entrance and measuring plane (MP) is z_{MP} . The distance between the virtual point source (VPS) and the measuring plane is z_{VPS} . F_{total} is the flux profile of the scattered beam with standard deviation σ_{total} . The experimental setup exhibits cylindrical symmetry with respect to the z -axis. The point labeled as $z_{MP,0}$ is located at a distance z_{MP} from the origin of coordinates.

where r is the radial distance measured from the beam axis, A_{total} and $A_{initial}$ are the scaling parameters, and $r_{c_{total}}$ and $r_{c_{initial}}$ are the center corrections.

The deconvolution of the two spatial profiles is the anti-Fourier transform of the division of the Fourier transformed fitted 1D normal distributions $F_{total}(r)$ and $F_{initial}(r)$. The anti-Fourier transform of two dividing Gaussian distributions is a Gaussian distribution whose variance is the difference of the individual variances^{23,24}

$$\sigma_0^2 = \sigma_{total}^2 - \sigma_{initial}^2, \quad (4)$$

where σ_{total}^2 is the spatial variance of the beam including air scatter contributions, the finite extension of the pencil beam, and the contributions of the respective scatterer, namely aluminum, brass, and lucite. $\sigma_{initial}^2$ is the spatial variance of the beam consisting of air scattering contributions and the finite extension of the pencil beam. Therefore, Eq. (4) yields the profile of a point like pencil beam impinging on the scatterer. Subsequent MCS with only scatter contribution in the measuring plane caused by the scatterer gives the variance σ_0^2 , the deconvolved flux of the beam profile

$$F_0(r) = \exp[-r^2/(2\sigma_0^2)]. \quad (5)$$

The spatial variance of the proton beam represented in Eq. (3) can be calculated using the Fermi–Eyges formalism.^{15,25–27} The spatial variance grows linearly with the correlation and quadratically with the angular variance. Due to the air in the experimental setup and the introduced scatterer, an additional integral term is added, which includes the scattering power T ²⁵

$$A_2(z) = A_{20} + 2A_{10}z + A_{00}z^2 + \int_0^z (z-z')^2 T(z') dz'. \quad (6)$$

In the Fermi–Eyges formalism, the variance of the spatial distribution of the proton pencil beam at a distance z is $2A_2(z)$. $2A_{10}$ is the covariance of the proton pencil beam at the origin plane. $2A_{00}$ is the variance of the angular distribution of the proton pencil beam at the same plane.^{15,25,26} The dependencies in Eq. (6), which determine the spatial variance of the proton pencil beam at a distance z from the origin (see Fig. 1) are uncorrelated. This is valid for sufficiently large distances z_{MP} and small values of $2A_{10}$ as compared to both z_{MP} and $2A_{00}$. Therefore, it is possible to deconvolve two normally distributed beam profiles, which differ only in the scattering term $\int_0^z (z-z')^2 T(z') dz'$, using the Eq. (4) given above.

A virtual point source (VPS) was used because the aforementioned deconvolution yielded a point-like pencil beam upstream of the scatterer.^{25,28} The virtual point source method is a corollary of the Fermi–Eyges theory. To calculate the distance between the virtual point source and the measuring plane z_{VPS} , the Fermi–Eyges formalism is used as follows.^{25,28}

$$z_{VPS} = z_{MP} - \frac{A_2(z_{MP})}{A_1(z_{MP})}, \quad (7)$$

where $2A_1(z_{MP})$ is the covariance of the proton pencil beam at the measuring plane. With the fluence profiles in five planes from the TOPAS simulations described in Section 2.C, $2A_2$ and $2A_1$ are calculated via a square fit.¹⁵ Using this method the virtual point source is determined for each combination of initial energy, scatterer material and scatterer thickness.

The virtual point source is used to calculate the angular distribution $F_i(\theta_i)$ that determines the experimental MCS angle. Each binned value of r , namely r_i , can be associated to a binned angle as⁷

$$\theta_i = \arctan\left(\frac{r_i}{z_{\text{VPS}}}\right). \quad (8)$$

The binned flux is obtained as

$$F_i(r_i) = \frac{z_{\text{VPS}}^2 + r_i^2}{z_{\text{VPS}}^2} F_0(r_i), \quad (9)$$

where Eq. (9) corrects for the inverse square law, due to the fact that the beam profiles were measured at a plane and not over a sphere. Applying again the fit of the normal distribution to θ_i , the resulting angular distribution in conjunction with the flux $F_i(\theta_i)$ is

$$F_i(\theta_i) = \exp[-\theta_i^2 / (2\theta_0^2)], \quad (10)$$

yielding θ_0 . The same procedure described above is followed for the RayStation Monte Carlo and the RayStation Pencil Beam Algorithm yielding θ_{RSMC} and θ_{RSPBA} .

The validity of the implementation of the deconvolution was tested using TOPAS. The setup in this validation was the same as that used in all Monte Carlo simulations described in Section 2.C, with the exception of the source, which was replaced by the extended source employed in the work of Verbeek *et al.*¹⁵ at 160 MeV. Thereby the source coincided with the one in the experiments. In a second simulation, an extended source without scatterer was placed in air at the same position as in the previous one. In both simulations the proton fluence was tallied at the z_{MP} distance from the upstream side of the scatterer. Using Eq. (4), σ_0 was then calculated from the fluence profiles.

2.C. Monte Carlo simulations

To calculate the MCS angles with the actual mean energy and energy spread of our facility proton beam, it was necessary to run TOPAS and PENH simulations that reproduce the commissioned beam. Energy and spread have been adjusted to reproduce the measured depth dose curves following the methods of Bortfeld and Bray,²⁹ Clasié,³⁰ and Grassberger.³¹ These experiments were performed with the plane parallel Bragg peak chamber (PTW, Freiburg, Germany).³² Unlike TOPAS and PENH, these adjustments were not done for RayStation. The beam model is calculated automatically by the system. The energy spectrum of a pencil beam in RayStation is determined by the discrete deconvolution of the respective depth dose curves.

2.C.1. Simulation and analytical calculation settings common to all codes

All Monte Carlo codes and the analytical RayStation Pencil Beam Algorithm were executed using the same material definition (Table I). The material compositions used in the LOOKUP software correspond to the material compositions used in experiments and Monte Carlo simulations. In the case of brass, there is a slight difference in composition between that one experimentally employed and the one appearing in

the LOOKUP software. The density variation between both compositions has been taken into account as uncertainty in the experimental data (see Section 2.D).

TOPAS and PENH use different electromagnetic stopping powers, depending on the materials. The stopping powers in TOPAS correspond to those given by the National Institute of Standards and Technology (NIST). The NIST electromagnetic stopping powers for aluminum, brass, and lucite were taken from the ICRU Report 49.³³ A test simulation in PENH was performed in which the TOPAS stopping powers were employed in the most challenging case, that is for 20 cm of lucite with a 220 MeV beam. The MCS angles agreed within 0.1% compared to a calculation with the default PENH stopping power tables.

The mean excitation energy of aluminum was set to 166.0 eV according to ICRU 90.³⁴ The aluminum used in the experiments is an alloy that has a magnesium admixture of 4.5% and a manganese admixture of 0.7%. The density of the alloy is 0.03 g/cm³ smaller than that of pure aluminum quoted in Table I. The difference has been considered in the uncertainty analysis (Section 2.D). The stopping powers differ by 0.01 eV, according to the Bragg additivity rule.³⁵ The mean excitation energy of lucite was set to 74.0 eV according to the pstar database given by the NIST. The mean excitation energy of brass was also calculated using the Bragg additivity rule.

No variance-reduction techniques were applied in the Monte Carlo simulations. Monte Carlo results are reported according to the RECORDS recommendations.³⁶

2.C.2. PENH parameter control and simulations

PENH classifies collisions into hard and soft on the basis of a mixed simulation scheme. The global effect of soft collisions between two consecutive hard interactions is described by using a multiple-scattering approach that reproduces the first and second moments of the angular and energy distributions. Hard interactions are simulated from the restricted differential cross sections. Inelastic collisions are described from a generalized oscillator strength (GOS) model with parameters defined to reproduce the high-energy stopping power. Elastic collisions are simulated from differential cross sections calculated with the eikonal approximation. The phase of the scattered wave is evaluated from a semi-classical approximation to the scattering wave function assuming small trajectory deflections. Additionally, the eikonal phase corrections of Wallace are employed. A correction to account for the final size of the nucleus is included.³⁷

Transport parameters are used to control the particle simulation in PENH. In what follows, the function of each parameter is briefly described. Parameters whose name ends with an ‘‘H’’ refer to protons, while those without refer to electrons and positrons. C1 and C1H are the average angular deflections produced by multiple elastic scattering along a path length equal to the mean free path between successive hard elastic events. C2 and C2H are the maximum average fractional energy losses between successive hard elastic events.

The cutoff energy values for hard inelastic collisions are WCC and WCCH. The limit energy value for the bremsstrahlung emission is WCR. Bremsstrahlung emission for protons is negligible at therapeutic energies and therefore not included. The EABS values are four thresholds that determine when particles are absorbed and the kinetic energy of photons, electrons, positrons or protons is deposited locally. These parameters are explained in detail in the PENELOPE User's Manual.¹⁷ Table II shows the transport parameters chosen for all materials. To achieve a spatial resolution of 10^{-14} cm, the EABS were chosen as indicated in Table II following the continuous slowing down approximation from the NIST data for the respective material. The other parameters in Table II were set according to Verbeek et al.¹⁵

The PENH simulations used a point-like pencil beam source with mean energy and energy spread in accordance with the facility beam. The source was located 50 cm away from the upstream surface of the scatterer in vacuum. On the downstream surface of the scatterer, a proton phase-space file (PSF) was tallied. For each simulation in PENH 10⁷, primary particles were sampled. The simulations were conducted on the Contessa computation cluster consisting of seven Intel(R) Xeon(R) CPU E5-2670 v3 @ 2.30 GHz (48 cores) with 64.0 GB RAM each. The most time-consuming simulation occurred in the case of 220 MeV for brass with a t_p of 0.8, which required 7.08×10^6 s/core.

The PSF data were subsequently used to determine the polar angle θ , with respect to the z -axis, of each proton. The resulting angular distribution was discretized in n bins and each bin was weighted with the annulus $1/\pi(\theta_n^2 - \theta_{n-1}^2)$. The resulting distribution was fitted to a normal distribution to obtain θ_p .

2.C.3. TOPAS parameter control and simulations

In TOPAS the transport parameter EMRangeMin was set to 100 eV for all particles. The production cut for all secondary particles was set to 10^{-14} cm according to Wulff et al.³⁸ corresponding to the above-mentioned range for the PENH simulations. The overall allowed maximum step size for the condensed history algorithm in TOPAS was set to 0.1 cm. The following physics packages were used in accordance to Zacharitou et al.³⁹: *g4em-standard_opt4*, *g4h-phy_QGSP_BIC_HP*, *g4decay*, *g4ion-binarycascade*, *g4h-elastic_HP*, and *g4stopping*. The *G4EmStandardPhysics_opt4* is used to include the *G4WentzelVIModel* for proton MCS

that provides multiple Coulomb physics in Geant4, yielding a better fit to experimental data according to Makarova et al.⁶ and Fuchs et al.¹¹

The selected transport parameters are more stringent than the default values. To assess their necessity, a test simulation using a lucite scatterer thickness of 20 cm and an initial beam energy of 220 MeV was run employing the default parameters. The MCS angles derived from both simulations differed by 0.8%, a value larger than the statistical uncertainty reached in all simulations presented herein.

The dR/R value determines the allowed energy loss per condensed history step. If the energy loss in the calculated condensed history step is too large, the step size is shortened in order not to exceed the maximum allowed energy loss. The maximum allowed energy loss is given by the ratio of the energy-dependent allowed range loss dR to the actual path length in the continuous slowing down approximation R of the considered particle. Processes such as the generation of secondary particles, border crossing or the overall allowed maximum step size can also interrupt the condensed history algorithm. The dR/R value was altered within the *g4em-standard_opt4* package inside Geant4. This value was originally set to 10% and changed to 5%, 0.5% and 0.005%. In all cases, compatible results for dR/R were found within a standard statistical uncertainty of 0.1%. Therefore, the value of 10% for dR/R was employed which produced simulations running five times faster than those in which a dR/R of 0.005% was used.

The setup of the simulations in TOPAS was equivalent to that in PENH. In addition to the PSF tallies, the proton fluences were tallied in vacuum using TOPAS at five planes downstream of the PSF to calculate the VPS. The fluence was tallied in 200 cylindrical bins of radial size of 0.1 cm. The most time-consuming simulation required 3.63×10^5 s/core. The analysis of the PSF files was analogous to the analysis of the PSFs simulated with PENH.

2.C.4. Multiple Coulomb scattering implementation in RayStation

RayStation Monte Carlo uses screened Rutherford cross sections adapted from the work of Kawrakow and Bielajew⁴⁰ based on Goudsmit-Saunderson.⁴¹ The RayStation Pencil Beam Algorithm uses the Rossi and Greisen scattering formula in the Fermi-Eyges formalism.²⁷ To achieve a better fit to experimental observations of proton beam widening in

TABLE II. Transport parameters for the PENH simulations.

| PENH transport parameters | | | | | | |
|---------------------------|----------------------|----------------------|------------|------------|-----------|-----------|
| EABS (γ) [keV] | EABS (e^-) [keV] | EABS (e^+) [keV] | C1 | C2 | WCC [keV] | WCR [keV] |
| 10.0 | 10.0 | 10.0 | 0.01 | 0.01 | 1.0 | 1.0 |
| EABS (p) [keV] | C1H | C2H | WCCH [keV] | WCRH [keV] | | |
| 100.0 | 0.01 | 0.01 | 1.0 | 1.0 | | |

water, the parameter E_s in the Rossi formula was modified by RayStation developers ($E_s = 18$ MeV instead of 21 MeV).¹³

To determine the MCS angle used for aluminum, brass and lucite in RayStation Monte Carlo and in the RayStation Pencil Beam Algorithm, a new beam model was commissioned. The considered scatterers were implemented as range shifters within this beam model. Since in RayStation quantities cannot be scored in vacuum, it was necessary to define a thin slice of air in the region of interest to allow for calculation of a dose profile. The z_{MP} (Fig. 1) was 67.5 cm. For each simulation in RayStation Monte Carlo 10^9 primary particles were sampled.

2.D. Uncertainty analysis

Experimental uncertainties were estimated according to the guidelines published by the Joint Committee for Guides in Metrology.⁴² These uncertainties result from facility-dependent fluctuations in the beam properties, manufacturing inaccuracies of the scatterers, detector properties, and the experimental setup. Facility-dependent uncertainties account for fluctuations of the spot size (0.27%) and the range (0.05 MeV) of the proton beam. Uncertainties related to the scatterers comprise the manufacturing spatial tolerance (0.05 cm) and possible density variations (0.04 g/cm³). The spatial Lynx PT detector uncertainty was taken as 0.02 cm according to the work of Grevillot et al.²¹ The positioning accuracy of the Lynx PT was estimated as 0.05 cm.

Although not strictly an experimental uncertainty, the uncertainty of the position of the source point within the scatterer has to be taken into account. In addition to the VPS, the so-called effective scattering point according to the ICRU Report 35 terminology²⁸ was calculated using the LOOKUP software. Subsequently, MCS angles were calculated employing both scattering point approaches. Despite the small difference between the two source locations compared to z_{MP} ,²⁵ the difference of these MCS angles was considered as uncertainty.

With the exception of the uncertainty related to the spot size, which was supposed to be a normally distributed type A uncertainty, the other were regarded as type B with an underlying rectangular distribution. By using the coverage factor $k = \sqrt{3}$, the corresponding standard deviation was determined. The effect of each uncertainty on the MCS angle was determined using the LOOKUP software. A linear dependence for each sensitivity coefficient was assumed. The sensitivity coefficient expresses the percentage contribution of a given source of uncertainty to the total uncertainty associated to the MCS angle. It was assumed that the uncertainties are uncorrelated. The combined absolute uncertainties are given in Tables III, A1, and B1. As the number of primary histories within the RayStation Monte Carlo simulations is high enough to reach a standard statistical uncertainty $< 0.001\%$, the uncertainties given for $\theta_{RS_{MC}}$ result only from the differences between the virtual point source and the effective scattering point. The same holds for the analytical $\theta_{RS_{PBA}}$. The average standard statistical uncertainty of the Monte Carlo

TABLE III. Average absolute deviations of multiple Coulomb scattering angles between: measured and simulated; measured and analytical Molière/Fano/Hanson (MFH); measured and RayStation Pencil Beam Algorithm (PBA). The deviations are averaged over all thicknesses of each given material. The standard statistical uncertainty of all quantities in the table related to Monte Carlo codes is 0.3%.

| | 100 MeV $\Delta_{\theta_0}[\%]$ | 160 MeV $\Delta_{\theta_0}[\%]$ | 220 MeV $\Delta_{\theta_0}[\%]$ |
|---------------|------------------------------------|------------------------------------|------------------------------------|
| Al | | | |
| PENH | 1.9 | 3.2 | 3.1 |
| TOPAS | 2.7 | 3.0 | 2.8 |
| RS MC | 2.8 | 3.3 | 3.2 |
| RS PBA | 2.9 | 1.7 | 1.6 |
| MFH | 2.3 | 2.4 | 1.9 |
| Brass | | | |
| PENH | 6.1 | 2.3 | 1.1 |
| TOPAS | 7.2 | 4.0 | 3.0 |
| RS MC | 5.6 | 1.8 | 2.3 |
| RS PBA | 5.8 | 6.9 | 6.1 |
| MFH | 7.9 | 5.0 | 4.0 |
| Lucite | | | |
| PENH | 1.2 | 2.7 | 2.4 |
| TOPAS | 2.5 | 3.6 | 2.8 |
| RS MC | 1.3 | 3.0 | 2.5 |
| RS PBA | 4.1 | 5.0 | 6.6 |
| MFH | 1.4 | 1.7 | 1.8 |

simulations was in all cases smaller than 0.1% on the calculation of the MCS angle using PENH and TOPAS.

3. RESULTS

The deconvolution methodology employed, as explained in Eq. (4), was tested in TOPAS Monte Carlo and produced deviations in the spot size of the beam ($\sqrt{2A_2}$), smaller than 0.001%. Simulated and measured depth doses agreed within ± 0.02 cm at R_{80} .

The measured and simulated scattering angles, as well as the results published by Gottschalk et al. are shown in Figs. 2 and 3. The experimental data of Gottschalk and co-workers, and ours are statistically compatible and the average deviation on the central values is 3% with a maximum deviation below 6%. As the measured thicknesses do not coincide with the ones from Gottschalk et al., the differences in the lower parts of the plots in Figs. 2 and 3 are calculated employing a linear point-to-point interpolation between the experimental θ_0 . A comparison with lucite was not possible because the scatterer thicknesses employed by Gottschalk and co-workers were outside the range of the thicknesses studied herein.

In Fig. 2, the MCS angles for aluminum are presented. The Monte Carlo codes PENH, TOPAS, and RayStation MC show similar behavior. The θ_P , θ_T , and $\theta_{RS_{MC}}$ of the three codes underestimate the θ_0 at the lowest energy up to a mean relative thickness of $t_\rho = 0.67$. At larger scatterer thicknesses,

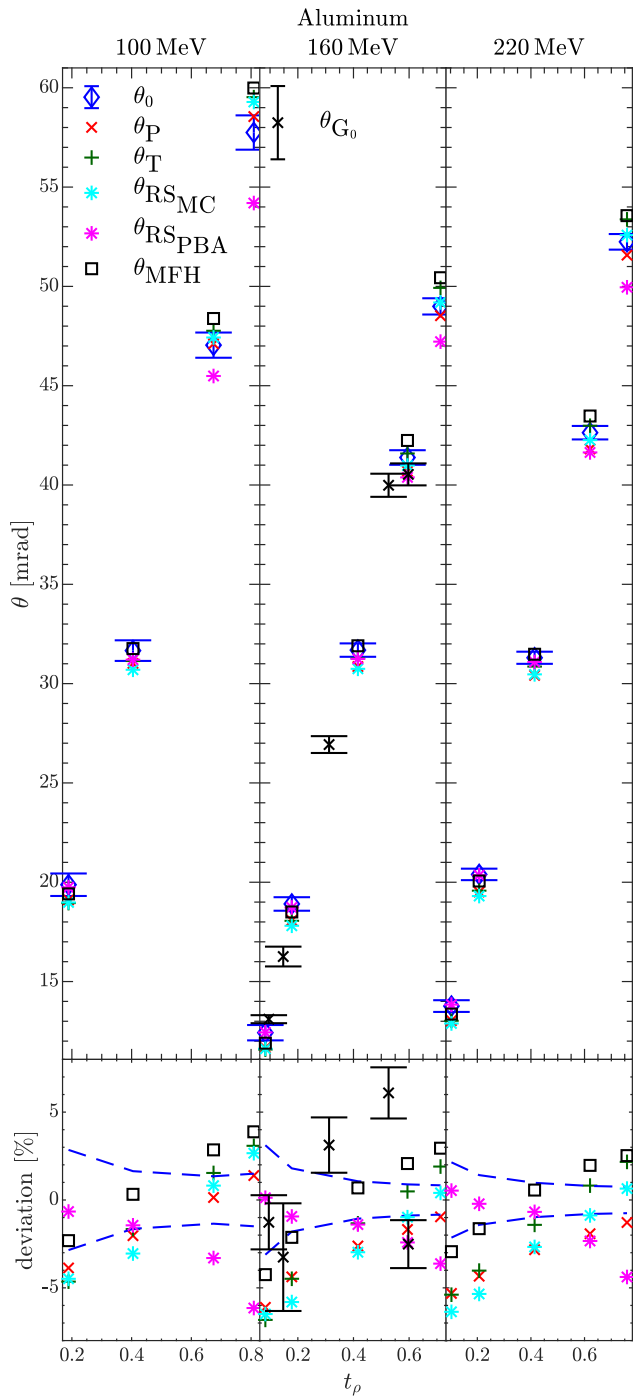


FIG. 2. MCS angles in aluminum. The upper plots show the MCS angles, while the lower plots show the deviations from the experimental measurements. The MCS angles are indicated by the respective subscripts. θ_0 , θ_P , θ_T , $\theta_{RS_{MC}}$, $\theta_{RS_{PBA}}$, and θ_{MFH} are the measured, PENH, TOPAS, RayStation Monte Carlo, RayStation Pencil Beam Algorithm, and Molière /Fano/Hanson MCS angles. The absolute uncertainty of the experimental data is indicated by a standard uncertainty bar. The dashed blue line indicates the standard uncertainty of the confidence interval of the experimental data. The standard statistical uncertainties of the Monte Carlo simulations are in all cases smaller than 0.1%, and therefore smaller than the symbol sizes used. For the case of 160 MeV a comparison with the experimental data of Gottschalk et al.⁷ is shown (θ_{G_0}). The differences between the experiment of this work and the one from Gottschalk et al. were determined by a linear interpolation and appear in the corresponding lower plot. t_ρ is the quantity resulting from Eq. (1).

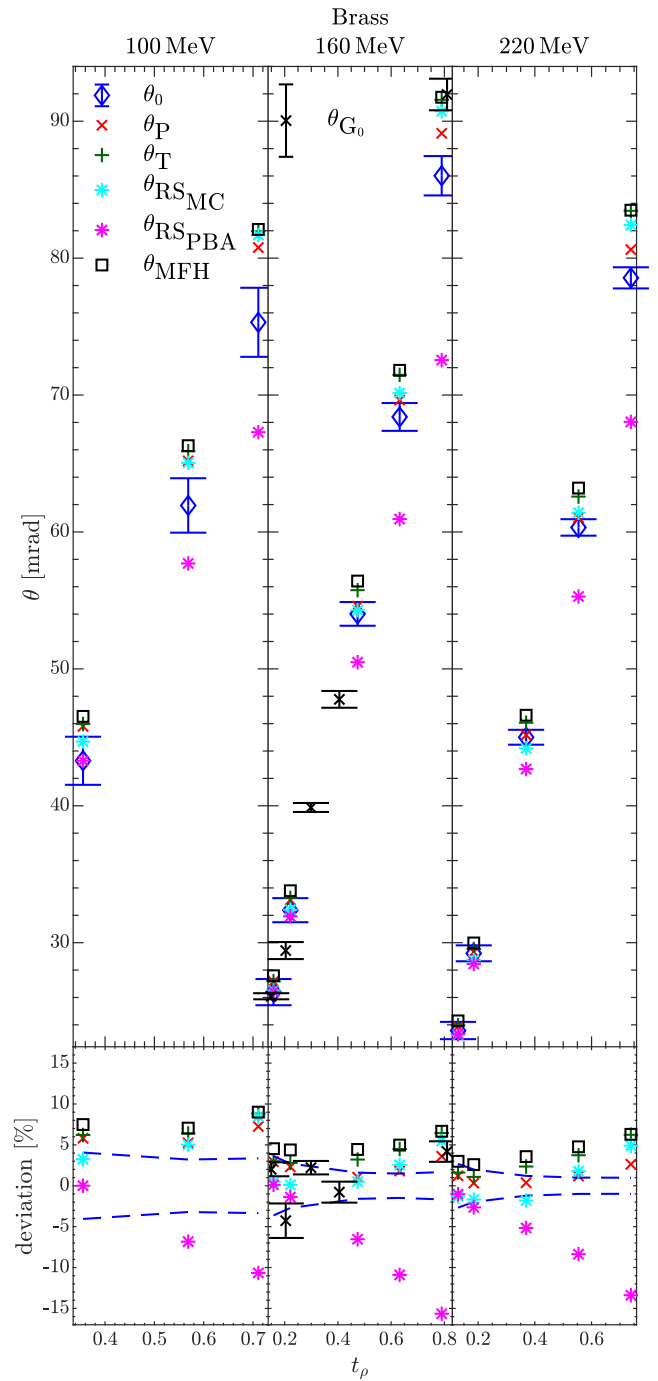


FIG. 3. MCS angles in brass. The upper plots show the MCS angles, while the lower plots show the deviations from the experimental measurements. The MCS angles are indicated by the respective subscripts. θ_0 , θ_P , θ_T , $\theta_{RS_{MC}}$, $\theta_{RS_{PBA}}$, and θ_{MFH} are the measured, PENH, TOPAS, RayStation Monte Carlo, RayStation Pencil Beam Algorithm, and Molière/Fano/Hanson MCS angles. The absolute uncertainty of the experimental data is indicated by a standard uncertainty bar. The dashed blue line indicates the standard uncertainty of the confidence interval of the experimental data. The standard statistical uncertainties of the Monte Carlo simulations are in all cases smaller than 0.1%, and therefore smaller than the symbol sizes used. For the case of 160 MeV a comparison with the experimental data of Gottschalk et al.⁷ is shown (θ_{G_0}). The differences between the experiment of this work and the one from Gottschalk et al. were determined by a linear interpolation and appear in the corresponding lower plot. t_ρ is the quantity resulting from Eq. (1).

however, the Monte Carlo codes overestimate the experimental data. This behavior shifts with increasing energy. The θ_p , θ_T , and $\theta_{RS_{MC}}$ are smaller than the experimental data up to relative thicknesses of 0.6 at 160 MeV, and up to 0.7 at 220 MeV. The differences between the Monte Carlo codes and the experimental data are the smallest in the medium scatterer thicknesses. The θ_{MFH} calculated with the analytical code Molière/Fano/Hanson (MFH) shows a similar behavior, but has an additional shift toward larger MCS angles. In contrast, the $\theta_{RS_{PBA}}$ calculated with the analytical RayStation Pencil Beam Algorithm agrees with the experimental data at low scatterer thicknesses and deviates in a negative direction with increasing scatterer thickness by up to 6.1% in the case of $t_p = 0.81$ at 100 MeV. The maximum deviation from the experimental MCS is 6.6% in the case of TOPAS at 160 MeV at the lowest scatterer thickness $t_p = 0.08$. The mean deviations for all codes from θ_0 are shown in Table II. These deviations were averaged over all thicknesses for each given material and energy. From Table III, it can be seen that the RayStation Monte Carlo algorithm shows on average the largest deviations from the experimental data in the case of aluminum, while the RayStation Pencil Beam Algorithm shows the smallest deviations from the measurements. The individual measured and simulated MCS angles for aluminum are given in detail in the Table A1 with their respective uncertainties.

The results of MCS in brass are presented in Fig. 3. The Monte Carlo codes and Molière/Fano/Hanson behave similarly. In contrast to aluminum, the experimental MCS angles are overestimated, especially in the case of 100 MeV. θ_p , θ_T , $\theta_{RS_{MC}}$, and θ_{MFH} show deviations in the positive direction from the measured MCS angles at low scatterer thicknesses, decreasing with increasing scatterer thickness to a relative minimum at $t_p = 0.57$ in the case of 100 MeV, $t_p = 0.47$ in the case of 160 MeV and $t_p = 0.37$ in the case of 220 MeV. The differences between the above-mentioned codes and the measurements are the smallest at these scatterer thicknesses. Subsequently, the differences between the Monte Carlo codes and Molière/Fano/Hanson, and the experimental data increase up to a maximum deviation of 9.5% at $t_p = 0.71$ and 100 MeV for θ_{MFH} . The analytical RayStation Pencil Beam Algorithm behaves in brass similar to the case of aluminum. Increasing scatterer thicknesses at each energy cause increasing deviations in negative direction between $\theta_{RS_{PBA}}$ and θ_0 reaching a maximum deviation of 15.6% at $t_p = 0.79$ and 160 MeV. On average, PENH and RayStation Monte Carlo show the smallest deviations from the measured MCS angles, while the RayStation Pencil Beam Algorithm differs most from the experimental results (Table III). The individual measured and simulated MCS angles for aluminum are given in detail in the Table B1 with their respective uncertainties.

Figure 4 presents the MCS angles for lucite. The discrepancies between the Monte Carlo codes and Molière/Fano/Hanson, and the experimental measurements are comparable to the results for aluminum. However, the differences between the Monte Carlo codes and

Molière/Fano/Hanson, and the experimental measurements become smaller with increasing thickness. Among PENH, TOPAS, RayStation Monte Carlo, and Molière/Fano/Hanson, the maximum deviation of TOPAS from experimental data is 7.2% at $t_p = 0.14$ in the case of 160 MeV. In contrast, the RayStation Pencil Beam Algorithm has a general average overestimation of 5.2% with respect to experiment (Table III). With increasing scatterer thickness, the discrepancy between the $\theta_{RS_{PBA}}$ and the θ_0 decreases to a minimum value of 1.9% at $t_p = 0.75$ in the case of 100 MeV. The RayStation Pencil Beam Algorithm deviates by a maximum of 7.7% at $t_p = 0.11$ in the case of 220 MeV. It is worth mentioning that the other analytical model under consideration, namely, Molière/Fano/Hanson also presents a deviation from the experimental results. However, the maximum deviation of the results obtained with Molière/Fano/Hanson amounts to 4%, occurring at 160 MeV in lucite. On average, the MCS angles calculated with Molière/Fano/Hanson show the smallest deviations from the measured MCS angles, while the RayStation Pencil Beam Algorithm exhibits the largest discrepancies with respect to experimental data as compared with the other codes (Table III). The measured, simulated and calculated lucite MCS angles are shown in detail with their respective uncertainties in Table C1 in the appendix.

The combined maximum uncertainty of the experimental data was below 4%. The combined average uncertainty of the experimental data was 1.8%. PENH, TOPAS, and RayStation Monte Carlo deviate by 2.5%, 3.4%, and 2.8% averaged over all energies, materials and thicknesses. The average deviations of the analytical RayStation Pencil Beam Algorithm and the Molière/Fano/Hanson model amount to 4.5% and 2.9%, respectively. RayStation Monte Carlo and the RayStation Pencil Beam Algorithm differ among themselves on average by 6.8%.

4. DISCUSSION

The results from Gottschalk and co-workers on aluminum and brass are statistically compatible with the ones presented herein (Figs. 2 and 3). An advantage of the deconvolution methodology employed in this work is that there is no risk of misalignment regarding the position of the proton beam and the pinhole apertures as occurs in the work of Gottschalk et al. Due to the deconvolution and the chosen detector, the experiments performed here were independent of the lateral position of the detector. In addition, a possible contamination of measured MCS angles by scattering within the collimator is excluded. Furthermore, the proton beam has a point source due to the deconvolution of F_{total} with $F_{initial}$, eliminating the need for accurate phase space modeling, such as in Huang et al.⁴³ No residuals were found due to deviations from a normally distributed proton beam.

The results yielded by the Molière/Fano/Hanson analytical model show an agreement with the experimental values with

an overall average deviation of 2.9%. The Molière/Fano/Hanson accuracy is reduced for target thicknesses $\geq 97\%$ ⁷ of the mean range of the protons. Since none of the thicknesses used come close to this, Molière/Fano/Hanson's accuracy is not affected.

The detailed uncertainty analysis took into account the various influences on the experimental determination of the MCS angles listed in Section 2.D. The aluminum was modeled as a pure material in the simulations and analytical calculations to facilitate comparison with other values reported in literature. The effect on the MCS angle produced by using pure aluminum in the simulations instead of the aforementioned alloy was investigated using TOPAS in the most demanding case. When the scatterer thickness was set to 11 cm and the energy to 220 MeV, the difference between the pure aluminum and the alloy was 0.1% on the MCS angle.

In the studies of Makarova et al. and Fuchs et al.,^{6,11} the experimental results of Gottschalk et al.⁷ served as reference. The simulated MCS angles of Fuchs et al. showed the smallest differences between the measured angles of Gottschalk et al. and the simulations for the *G4WentzelVIModel* in Geant4, which is in agreement with the results of Makarova et al. For the *G4WentzelVIModel* simulated MCS angles, Fuchs and co-workers show deviations from the data of Gottschalk and co-workers of $\pm 5\%$, with an average deviation of -2% in the range of thicknesses presented herein in the case of aluminum at 160 MeV. The differences between the θ_T and the θ_{G_0} were determined by a linear interpolation and lie between -5.9% and 3.1% with an average deviation of -3.0% . Thus the results in this work are consistent with the results obtained by Fuchs et al. The differences between Fuchs et al. and Gottschalk et al. were taken from the graphs in Fig. 2 in the work of Fuchs and co-workers. Only the values of t_ρ that match the range of those simulated herein were compared.

In accordance with the statement of Fuchs and co-workers, and Gottschalk and co-workers, MCS angles simulated in high Z materials, such as brass, tend to be larger than the corresponding experimental values. This is also confirmed by the results of Makarova and co-workers. They describe that their simulated brass MCS angles are on average 4% too high for the case of 160 MeV which fits to the average deviation at that energy in this work (Table III). TOPAS, PENH and RayStation Monte Carlo follow this behavior.

Despite the fact that the Monte Carlo codes involved have different MCS implementations, they all give similar results. However, the RayStations Monte Carlo algorithm includes a uniform scaling factor of 0.93 to the scattering model of Kawrakow and Bielajew. This 7% correction was introduced to better comply with a dataset of beam widening measurements in water.¹³

The effect of the MCS angle on the spot size in a clinical scenario was investigated in TOPAS for a range shifter made of 5 cm lucite at an energy of 160 MeV with a clinically extended beam. The beam started 45 cm from the isocenter, propagated through the range shifter and a PSF was tallied at the downstream end of the scatterer. The beam properties of

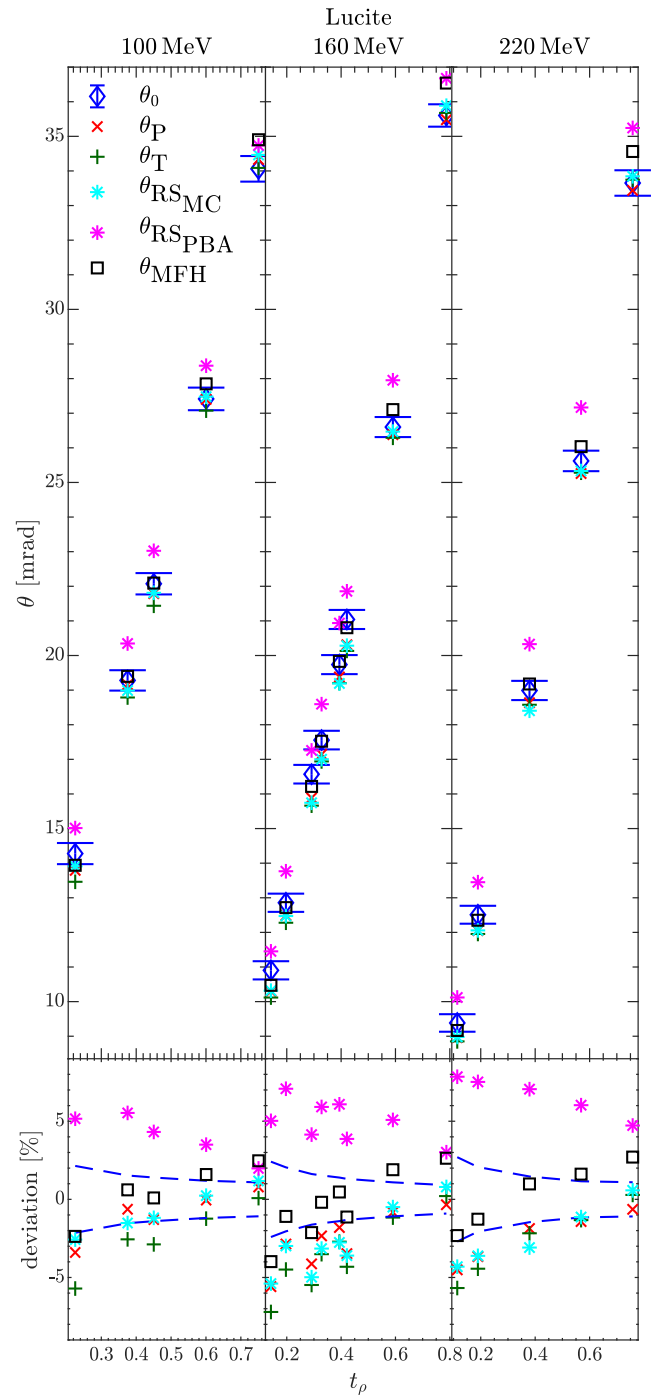


FIG. 4. MCS angles in lucite. The upper plots show the MCS angles, while the lower plots show the deviations from the experimental measurements. The MCS angles are indicated by the respective subscripts. θ_0 , θ_P , θ_T , $\theta_{RS_{MC}}$, $\theta_{RS_{PBA}}$, and θ_{MFH} are the measured, PENH, TOPAS, RayStation Monte Carlo, RayStation Pencil Beam Algorithm, and Molière/Fano/Hanson MCS angles. The absolute uncertainty of the experimental data is indicated by a standard uncertainty bar. The dashed blue line indicates the standard uncertainty of the confidence interval of the experimental data. The standard statistical uncertainties of the Monte Carlo simulations are in all cases smaller than 0.1%, and therefore smaller than the symbol sizes used. t_ρ is the quantity resulting from Eq. (1).

that PSF were modified by increasing the values of $\sqrt{2A_2}$ and the $\sqrt{2A_0}$ at the position of 5 cm both in 10%. Two simulations over a therapeutic air gap of 40cm were then performed

starting on the scatterer output. One with the increased beam properties and one with the unaltered beam properties. The comparison of the spot size demonstrated an increase of 10% on the value of $\sqrt{2A_2}$ at the isocenter. Thus, a deviation in the MCS angle has direct consequences on the spot size and results in inaccurate beam modelling. For example the work of Lin *et al.*⁴⁴ shows that inaccurate MCS in the case of TOPAS 1.0-beta 8 caused the primary spot size to be smaller by up to 15% in solid water.

This clinical scenario is valuable to estimate the effect of MCS angles on spot size. However, if the capability of the TPS is to be tested in relation to the calculation of the spot size and transport in air, it would be useful to consider large air gap geometries with the materials studied as a benchmark for any TPS, and Monte Carlo dose calculation tool. In addition, compared to clinical scenarios the MCS angle deviations herein are not mixed with other imperfections as it might be the case in a clinical scenario, where the reason for a difference in spot size can be masked by various influencing factors.

Another approach to measure the MCS angles would be the use of the AdvaPIX-TPX3 semiconductor sensor from the work of Granja *et al.* and Charyyev *et al.*^{45,46} The AdvaPIX-TPX3 measures directly the angles of the scattered protons, whereby the conversion of the spot profiles into an angular distribution by Eq. (8) is unnecessary. This bypasses the VPS approach which limits the accuracy of the Lynx PT detector compared to the semiconductor sensor. However, as it can be seen from the uncertainty analysis on the RayStation calculated MCS angles, the influence of the VPS on the general uncertainties is negligible. Furthermore, this effect was taken into account within the uncertainty analysis (see Section 2.D). In the present work, the novel approach for measuring MCS angles can be carried out with the usual detectors employed in radiation therapy, such as EBT3 film or diodes.

5. CONCLUSION

Simulations and experiments were conducted using pencil-beam spots of a proton therapy system to obtain MCS

angles for a combination of materials, energies, and thicknesses. Measured MCS angles for 160 MeV in aluminum and brass are statistically compatible to those found by Gottschalk and co-workers. The experimental method developed herein allows measuring MCS angles in clinical facilities with similar accuracy to that obtained in research beamlines. Our methodology permits to extend the database on experimental MCS angles which is rather limited. This work further provides benchmark data for lucite in thicknesses relevant for clinical applications. The agreement between PENH, TOPAS, RayStation Monte Carlo, the Molière/Fano/Hanson theory and the experiments is satisfactory. PENH, TOPAS and RayStation Monte Carlo deviate by 2.5%, 3.4%, and 2.8% averaged over all energies, materials and thicknesses. The RayStation Pencil Beam Algorithm shows larger deviations from the experimental results compared to Molière/Fano/Hanson. The average deviations of the analytical RayStation Pencil Beam Algorithm and the Molière/Fano/Hanson model amount to 4.5% and 2.9%, respectively.

ACKNOWLEDGMENT

NV, JW, CB, BT, and LB are thankful to the HARMONIC project. The HARMONIC project (Health effects of cardiac fluoRoscopy and MODern radIotherapy in paediatricCs) has received funding from the Euratom research and training programme 2014-2018 under grant agreement No 847707. NV, JW, CB, and LB acknowledge support from the Spanish Junta de Andalucía under grant agreement P18-RT-3237.

CONFLICTS OF INTEREST

MJ discloses that he is an employee of RaySearch. The rest of the authors have no conflict to disclose.

AVAILABILITY OF DATA

The data that support the findings of this study are available from the corresponding author upon reasonable request.

APPENDIX A

A MULTIPLE COULOMB SCATTERING IN ALUMINUM

TABLE A1. Measured θ_0 and simulated θ_P , θ_T , and $\theta_{RS_{MC}}$ MCS angles from the Monte Carlo codes PENH, TOPAS, and RayStation Monte Carlo together with the $\theta_{RS_{PBA}}$ and θ_{MFH} from the analytical codes RayStation Pencil Beam Algorithm and Molière/Fano/Hanson from the LOOKUP software in the case of aluminum. t_ρ is the quantity yielded by Eq. (1).

| Aluminum | | | | | | |
|----------------|-------------------|-------------------|---------------------------|----------------------------|-----------------------|-------------------|
| t_ρ | θ_P [mrad] | θ_T [mrad] | $\theta_{RS_{MC}}$ [mrad] | $\theta_{RS_{PBA}}$ [mrad] | θ_{MFH} [mrad] | θ_0 [mrad] |
| 100 MeV | | | | | | |
| 0.19 | 19.105 (2) | 18.950 (2) | 18.983 (1) | 19.743 (1) | 19.414 | 19.9 (6) |
| 0.40 | 31.018 (5) | 31.137 (5) | 30.696 (1) | 31.205 (1) | 31.763 | 31.7 (6) |
| 0.67 | 47.108 (15) | 47.765 (15) | 47.426 (1) | 45.488 (1) | 48.383 | 47.0 (7) |
| 0.81 | 58.549 (11) | 59.527 (11) | 59.284 (1) | 54.196 (1) | 59.987 | 57.7 (9) |
| 160 MeV | | | | | | |
| 0.08 | 11.665 (5) | 11.576 (5) | 11.617 (1) | 12.439 (1) | 11.896 | 12.4 (4) |
| 0.18 | 18.078 (2) | 18.057 (2) | 17.807 (3) | 18.728 (3) | 18.503 | 18.9 (4) |
| 0.42 | 30.858 (3) | 31.266 (3) | 30.745(1) | 31.245 (1) | 31.905 | 31.7 (4) |
| 0.59 | 40.689 (7) | 41.586 (7) | 40.979 (1) | 40.384 (1) | 42.242 | 41.4 (4) |
| 0.71 | 48.523 (12) | 49.924 (12) | 49.190 (1) | 47.218 (1) | 50.436 | 49.0 (5) |
| 220 MeV | | | | | | |
| 0.10 | 13.033 (3) | 13.023 (3) | 12.889 (3) | 13.838 (3) | 13.360 | 13.8 (3) |
| 0.21 | 19.510 (1) | 19.574 (1) | 19.304 (2) | 20.350 (2) | 20.061 | 20.4 (3) |
| 0.41 | 30.415 (12) | 30.858 (12) | 30.465 (2) | 31.089 (2) | 31.478 | 31.3 (4) |
| 0.62 | 41.815 (7) | 42.983 (7) | 42.259 (2) | 41.639 (2) | 43.473 | 42.6 (4) |
| 0.76 | 51.573 (23) | 53.375 (23) | 52.582 (4) | 49.954 (4) | 53.562 | 52.2 (4) |

B MULTIPLE COULOMB SCATTERING IN BRASS

TABLE B1. Measured θ_0 and simulated θ_P , θ_T , and $\theta_{RS_{MC}}$ MCS angles from the Monte Carlo codes PENH, TOPAS, and RayStation Monte Carlo together with the $\theta_{RS_{PBA}}$ and θ_{MFH} from the analytical codes RayStation Pencil Beam Algorithm and Molière/Fano/Hanson from the LOOKUP software in the case of brass. t_ρ is the quantity yielded by Eq. (1).

| Brass | | | | | | |
|----------------|-------------------|-------------------|---------------------------|----------------------------|-----------------------|-------------------|
| t_ρ | θ_P [mrad] | θ_T [mrad] | $\theta_{RS_{MC}}$ [mrad] | $\theta_{RS_{PBA}}$ [mrad] | θ_{MFH} [mrad] | θ_0 [mrad] |
| 100 MeV | | | | | | |
| 0.36 | 45.802 (42) | 45.976 (42) | 44.690 (1) | 43.290 (1) | 46.529 | 43 (2) |
| 0.57 | 65.185 (63) | 65.898 (63) | 65.049 (2) | 57.702 (2) | 66.302 | 62 (2) |
| 0.71 | 80.773 (104) | 81.965 (106) | 81.690 (1) | 67.285 (1) | 82.095 | 75 (3) |
| 160 MeV | | | | | | |
| 0.16 | 27.166 (25) | 27.181 (25) | 26.515 (1) | 26.419 (1) | 27.585 | 26 (1) |
| 0.22 | 33.121 (32) | 33.279 (32) | 32.409 (1) | 31.927 (1) | 33.794 | 32.4 (9) |
| 0.47 | 54.583 (58) | 55.748 (60) | 54.290 (1) | 50.486 (1) | 56.413 | 54.0 (9) |
| 0.63 | 69.631 (76) | 71.472 (78) | 70.139 (1) | 60.943 (1) | 71.804 | 68 (1) |
| 0.79 | 89.117 (142) | 91.561 (146) | 90.729 (1) | 72.554 (1) | 91.749 | 86 (2) |
| 220 MeV | | | | | | |
| 0.13 | 23.871 (21) | 23.964 (21) | 23.279 (2) | 23.342 (2) | 24.290 | 23.6 (7) |
| 0.18 | 29.320 (29) | 29.541 (29) | 28.731 (1) | 28.452 (1) | 29.981 | 29.2 (6) |
| 0.37 | 45.173 (48) | 46.065 (49) | 44.194 (2) | 42.682 (2) | 46.611 | 45.0 (6) |
| 0.55 | 61.045 (63) | 62.582 (64) | 61.405 (1) | 55.284 (1) | 63.205 | 60.3 (7) |
| 0.74 | 80.622 (85) | 83.455 (88) | 82.416 (1) | 68.043 (1) | 83.498 | 78.6 (8) |

C MULTIPLE COULOMB SCATTERING IN LUCITE

TABLE C1. Measured θ_0 and simulated θ_p , θ_T , and $\theta_{RS_{MC}}$ MCS angles from the Monte Carlo codes PENH, TOPAS, and RayStation Monte Carlo together with the $\theta_{RS_{PBA}}$ and θ_{MFH} from the analytical codes RayStation Pencil Beam Algorithm and Molière/Fano/Hanson from the LOOKUP software in the case of lucite. t_p is the quantity yielded by Eq. (1).

| Lucite | | | | | | |
|----------------|-------------------|-------------------|---------------------------|----------------------------|-----------------------|-------------------|
| t_p | θ_p [mrad] | θ_T [mrad] | $\theta_{RS_{MC}}$ [mrad] | $\theta_{RS_{PBA}}$ [mrad] | θ_{MFH} [mrad] | θ_0 [mrad] |
| 100 MeV | | | | | | |
| 0.23 | 13.792 (29) | 13.462 (29) | 13.910 (1) | 15.014 (1) | 13.939 | 14.3 (4) |
| 0.38 | 19.159 (36) | 18.787 (35) | 18.989 (1) | 20.347 (1) | 19.398 | 19.3 (3) |
| 0.45 | 21.787 (40) | 21.437 (40) | 21.812 (1) | 23.025 (1) | 22.093 | 22.1 (4) |
| 0.60 | 27.400 (53) | 27.075 (52) | 27.478 (2) | 28.373 (2) | 27.849 | 27.4 (4) |
| 0.75 | 34.331 (65) | 34.088 (65) | 34.462 (1) | 34.736 (1) | 34.902 | 34.1 (4) |
| 160 MeV | | | | | | |
| 0.14 | 10.295 (19) | 10.118 (19) | 10.317 (1) | 11.453 (1) | 10.470 | 10.9 (3) |
| 0.20 | 12.489 (26) | 12.279 (26) | 12.473 (1) | 13.767 (1) | 12.716 | 12.9 (3) |
| 0.29 | 15.886 (31) | 15.662 (30) | 15.745 (3) | 17.257 (3) | 16.218 | 16.6 (3) |
| 0.33 | 17.145 (32) | 16.940 (32) | 17.003 (1) | 18.594 (1) | 17.523 | 17.6 (3) |
| 0.39 | 19.381 (46) | 19.202 (45) | 19.193 (2) | 20.938 (2) | 19.830 | 19.7 (3) |
| 0.42 | 20.310 (38) | 20.133 (38) | 20.284 (1) | 21.855 (1) | 20.803 | 21.0 (3) |
| 0.59 | 26.381 (59) | 26.290 (59) | 26.469 (1) | 27.953 (1) | 27.105 | 26.6 (3) |
| 0.79 | 35.480 (70) | 35.677 (71) | 35.885 (2) | 36.676 (2) | 36.539 | 35.6 (4) |
| 220 MeV | | | | | | |
| 0.11 | 8.960 (17) | 8.851 (17) | 8.979 (2) | 10.120 (2) | 9.166 | 9.4 (3) |
| 0.19 | 12.051 (23) | 11.955 (23) | 12.058 (2) | 13.450 (2) | 12.351 | 12.5 (3) |
| 0.38 | 18.635 (35) | 18.577 (35) | 18.404 (4) | 20.329 (4) | 19.177 | 19.0 (3) |
| 0.57 | 25.258 (47) | 25.281 (47) | 25.331 (3) | 27.166 (3) | 26.035 | 25.6 (3) |
| 0.76 | 33.436 (75) | 33.747 (76) | 33.845 (7) | 35.242 (7) | 34.562 | 33.7 (4) |

^{a)}Author to whom correspondence should be addressed. Electronic mail: nico.verbeek@uk-essen.de.

REFERENCES

- Molière G. Theorie der Streuung schneller geladener Teilchen II Mehrfach- und Vielfachstreuung. *Z Naturforsch.* 1948;3:78–97.
- Fano U. Inelastic collisions and the molière theory of multiple scattering. *Phys Rev.* 1954;93:117.
- Hanson AO, Lanzl LH, Lyman EM, Scott MB. Measurement of multiple scattering of 15.7-MeV electrons. *Phys Rev.* 1951;84:634–637.
- Kanematsu N. Alternative scattering power for Gaussian beam model of heavy charged particles. *Nucl Instrum Meth B.* 2008;266:5056–5062.
- Gottschalk B. On the scattering power of radiotherapy protons. *Med Phys.* 2010;37:352–367.
- Makarova A, Gottschalk B, Sauerwein W. Comparison of Geant4 multiple Coulomb scattering models with theory for radiotherapy protons. *Phys Med Biol.* 2017;62:5959–5974.
- Gottschalk B, Koehler AM, Schneider RJ, Sisterson JM, Wagner MS. Multiple Coulomb scattering of 160 MeV protons. *Nucl Instrum Meth B.* 1993;74:467–490.
- Matysiak W, Yeung D, Slopsema R, Zuofeng L. Evaluation of the range shifter model for proton pencil-beam scanning for the Eclipse vol 11 treatment planning system. *J Appl Clin Med Phys.* 2016;17:391–404.
- Agostinelli S, Allison J, Amako K, et al. Geant4—a simulation toolkit. *Nucl Instrum Meth A.* 2003;506:250–303.
- Allison J, Amako K, Apostolakis J, et al. Geant4 developments and applications. *IEEE Trans Nucl Sci.* 2006;53:270–278.
- Fuchs H, Vatnitsky S, Stock M, Georg D, Greillot L. Evaluation of Gate/Geant4 multiple Coulomb scattering algorithms for a 160 MeV proton beam. *Nucl Instrum Meth B.* 2017;410:122–126.
- Perl J, Shin J, Schümann J, Faddegon B, Paganetti H. TOPAS: an innovative proton Monte Carlo platform for research and clinical applications. *Med Phys.* 2012;39:6818–6837.
- RaySearch Laboratories. RAYSTATION 9B Reference Manual. RaySearch Laboratories AB, Schweden; 2020.
- Salvat F, Quesada JM. Nuclear effects in proton transport and dose calculations. *Nucl Instrum Meth B.* 2020;475:49–62.
- Verbeek N, Wulff J, Bäumer C, Smyczek S, Timmermann B, Brualla L. Single pencil beam benchmark of a module for Monte Carlo simulation of proton transport in the PENELOPE code. *Med Phys.* 2020;48:456–476.
- Berger MJ. Monte Carlo calculation of the penetration and diffusion of fast charged particles. In: Alder B, Fernbach S, Rotenberg M, eds. *Methods in Computational Physics*, vol. 1. Cambridge, NY: Academic Press; 1963:135–215.
- Salvat F. PENELOPE-2018—A Code System for Monte Carlo Simulation of Electron and Photon transport. NEA/MBDAV/R(2019)1. ISSN 2707-2894. July 2019.
- Sempau J, Acosta E, Baro J, Fernandez-Varea JM, Salvat F. An algorithm for Monte Carlo simulation of coupled electron-photon transport. *Nucl Instrum Meth A.* 1997;132:377–390.
- Gottschalk B. 2014 Software (BGware.zip), including Windows executables, data files and Fortran source code, free download at <https://gray.mgh.harvard.edu/software/212-bgware>.
- Russo S, Mirandola A, Molinelli S, et al. Characterization of a commercial scintillation detector for 2-D dosimetry in scanned proton and carbon ion beams. *Phys Medica.* 2017;34:48–54.

21. Grevillot L, Stock M, Palmans H, et al. Implementation of dosimetry equipment and phantoms at the MedAustron light ion beam therapy facility. *Med Phys*. 2018;45:352–369.
22. Placidi L, Togno M, Weber DC, Lomax AJ, Hrbacek J. Range resolution and reproducibility of a dedicated phantom for proton PBS daily quality assurance. *Z Med Phys*. 2018;28:310–317.
23. Kanematsu N, Yonai S, Ishizaki A, Torikoshi M. Computational modeling of beam-customization devices for heavy-charged-particle radiotherapy. *Phys Med Biol*. 2008;53:3113.
24. Bäumer C, Fuentes C, Janson M, Matic A, Timmermann B, Wulff J. Stereotactical fields applied in proton spot scanning mode with range shifter and collimating aperture. *Phys Med Biol*. 2019;64:155003.
25. Gottschalk B. Techniques of proton radiotherapy: transport theory. *arXiv:1204.4470*; 2012.
26. Eyges L. Multiple scattering with energy loss. *Phys Rev*. 1948;74:1534–1535.
27. Rossi B, Greisen K. Cosmic-ray theory. *Rev Modern Phys*. 1941;13:240–315.
28. Dosimetry R. Electron beams with energies between 1 and 50 MeV (Report 35). *J ICRU*. 1984;63:48–51.
29. Bortfeld T, Bray TA. An analytical approximation of the Bragg curve for therapeutic proton beams. *Med Phys*. 1997;4:2024–2033.
30. Clasié B, Depauw N, Fransen M, et al. Golden beam data for proton pencil-beam scanning. *Phys Med Biol*. 2012;57:1147–1158.
31. Grassberger C, Lomax AJ, Paganetti H. Characterizing a proton beam scanning system for Monte Carlo dose calculation in patients. *Phys Med Biol*. 2015;60:633–645.
32. Bäumer C, Koska B, Lambert J, Timmermann B, Mertens T, Takoukam TP. Evaluation of detectors for acquisition of pristine depth-dose curves in pencil beam scanning. *J Appl Clin Med Phys*. 2015;16:151–163.
33. International Commission on Radiation Units and Measurements. Stopping power and ranges for protons and alpha particles (Report 49). *J ICRU*. 1993;49:107–183.
34. International Commission on Radiation Units and Measurements. Key data for ionizing-radiation dosimetry: measurement standards and applications (Report 90). *J ICRU*. 2014;90:33–34.
35. Bär E, Andreo P, Lalonde A, Royle G, Bouchard H. Optimized I-values for use with the Bragg additivity rule and their impact on proton stopping power and range uncertainty. *Phys Med Biol*. 2018;63:165007.
36. Sechopoulos I, Rogers DWO, Bazalova-Carter M, et al. RECORDS: improved Reporting of montE CarlO RaDiation transport studies: report of the AAPM Research Committee Task Group 268. *Med Phys*. 2018;45:e1–e5.
37. Salvat F. A generic algorithm for Monte Carlo simulation of proton transport. *Nucl Instrum Meth B*. 2013;316:144–159.
38. Wulff J, Baumann KS, Verbeek N, Bäumer C, Timmermann B, Zink K. TOPAS/Geant4 configuration for ionization chamber calculations in proton beams. *Phys Med Biol*. 2018;63:115013.
39. Zacharatou Jarlskog C, Paganetti H. Physics settings for using the Geant4 toolkit in proton therapy. *IEEE T Nucl Sci*. 2008;55:1018–1025.
40. Kawrakow I, Bielajew AF. Beam interactions with materials and atoms. *Nucl Instrum Meth B*. 1998;134:325–336.
41. Goudsmit SA, Saunderson JL. Multiple scattering of electrons. *Phys Rev*. 1940;57:24–29.
42. Joint Committee for Guides in Metrology. Evaluation of measurement data — Guide to the expression of uncertainty in measurement. JCGM. 100; 2008.
43. Huang S, Kang M, Souris K, et al. Validation and clinical implementation of an accurate Monte Carlo code for pencil beam scanning proton therapy. *J Appl Clin Med Phys*. 2018;19:558–572.
44. Lin L, Kang M, Solberg TD, Ainsley C, McDonough JE. Experimentally validated pencil beam scanning source model in TOPAS. *Phys Med Biol*. 2014;59:6859–6873.
45. Charyyev S, Chang CW, Harms J, et al. A novel proton counting detector and method for the validation of tissue and implant material maps for Monte Carlo dose calculation. *Phys Med Biol*. 2021; 66:045003.
46. Granja C, Jakubek J, Polanski S, et al. Resolving power of pixel detector Timepix for wide-range electron, proton and ion detection. *Nucl Instrum Meth A*. 2018;908:60–71.